




# Radio SLAM for 6G Systems at THz Frequencies: Design and Experimental Validation

Marina Lotti , *Graduate Student Member, IEEE*, Gianni Pasolini , *Member, IEEE*, Anna Guerra , *Member, IEEE*,  
 Francesco Guidi , *Member, IEEE*, Raffaele D'Errico , *Senior Member, IEEE*,  
 and Davide Dardari , *Senior Member, IEEE*

**Abstract**—Next-generation wireless networks will see the convergence of communication and sensing, also exploiting the availability of large bandwidths in the THz spectrum and electrically large antenna arrays on handheld devices. In particular, it is envisaged that user devices will be able to automatically scan their surroundings by steering a very narrow antenna beam and collecting echoes reflected by objects and walls. These data will be utilized to derive a map of the surrounding indoor environment and infer users' trajectories using simultaneous localization and mapping (SLAM) techniques. In this article, we address this scenario by proposing original radio-SLAM (R-SLAM) algorithms, derived from image processing techniques, to map the environment and pinpoint the device position in the map starting from measurements sensed by a mobile THz radar. Initially, to fully understand the THz backscattering phenomenon, we provide an experimental characterization of the THz backscattering channel in indoor environments. Then, the performance of the proposed algorithms is assessed using real-world THz radar measurements and is compared with state-of-the-art SLAM techniques, demonstrating the superiority of the proposed approaches.

**Index Terms**—6G Systems, Radio SLAM, THz Band, THz Backscattering Channel, Image Pose Registration, ISAC.

Manuscript received 9 December 2022; revised 12 April 2023; accepted 24 May 2023. Date of publication 12 June 2023; date of current version 13 October 2023. This work was supported in part by the HORIZON-JU-SNS-2022 EU Project TIMES under Grant 101096307, in part by the H2020 Project LOCUS under Grant 871249, in part by the European Union under the Italian National Recovery and Resilience Plan (NRRP) of NextGenerationEU, partnership on “Telecommunications of the Future” under Grant PE00000001 - Program RESTART), in part by SoBigData.it - Strengthening the Italian RI for Social Mining and Big Data Analytics under Grant Prot. IR0000013, and in part by the French ANR Project S2LAM. The guest editor coordinating the review of this manuscript and approving it for publication was Prof. Josep Miquel Jornet. (Corresponding author: Gianni Pasolini.)

Marina Lotti and Davide Dardari are with the Department of Electrical, Electronic and Information Engineering Guglielmo Marconi “Guglielmo Marconi”, University of Bologna, 47521 Cesena, Italy, and also with the WiLAB-CNIT, 40136 Bologna, Italy (e-mail: marina.lotti2@unibo.it; davide.dardari@unibo.it).

Gianni Pasolini is with the Department of Electrical, Electronic and Information Engineering Guglielmo Marconi “Guglielmo Marconi”, University of Bologna, 40136 Bologna, Italy, and also with the WiLAB-CNIT, 40136 Bologna, Italy (e-mail: gianni.pasolini@unibo.it).

Anna Guerra and Francesco Guidi are with the National Research Council of Italy, IEIT-CNR, 00185 Rome, Italy, and also with the WiLAB-CNIT, 47521 Cesena, Italy (e-mail: anna.guerra@cnr.it; francesco.guidi@cnr.it).

Raffaele D'Errico is with the CEA, LETI, MINATEC Campus, 38054 Grenoble, France, and also with the University of Grenoble-Alpes, 38000 Grenoble, France (e-mail: raffaele.derrico@cea.fr).

Digital Object Identifier 10.1109/JSTSP.2023.3285101

## I. INTRODUCTION

NEXT-GENERATION cellular networks are credited to becoming the point of convergence of communication and sensing thanks to the availability of high-frequency technologies that will foster the creation of an ecosystem of applications and services exploiting seamless connectivity and data rates at an unprecedented scale [1], [2]. In fact, unlike today's fifth generation (5G) networks, which are primarily designed for wireless communications, it is expected that sixth generation (6G) networks will entail a quantum leap towards the integration of sensing capabilities in handheld devices so that the latter will be fully aware of their surrounding 3D environment (integrated sensing and communication (ISAC)). In this regard, the ability to operate in the Terahertz (THz) band is expected to play a crucial role, as the wide bandwidth available will result in high spatial resolution, and the feasibility of large antenna arrays will enable unprecedented angular resolution [3], [4], [5], [6], [7].

Traditionally, the THz band, namely the frequencies in the range 0.1 – 10 THz, has represented the *last gap* between radio and optical signals [8], [9]. In the past, the THz gap was due to the challenges associated with developing hardware (such as transceivers and antennas) capable of delivering satisfactory performance at these frequencies. However, the situation is rapidly changing as technological obstacles are being overcome. New applications and services that require tight integration of sensing and communications capabilities are thus becoming possible [10], [11]. From this perspective, mobile devices are poised to become exceptional tools for environmental monitoring, leveraging their widespread adoption and the growing integration of embedded sensors [12]. However, their potential extends even further: according to the 6G vision, handheld devices are expected to revolutionize our perception of indoor environments and enhance our mobility within them. These devices will autonomously create digital maps of our surroundings and accurately pinpoint our position within the map, without relying on a dedicated positioning infrastructure [12]. This perspective motivated our work, which proposes original SLAM algorithms working on THz signals and evaluates their performance when fed with real measurements taken in an indoor scenario.

Currently, accurate SLAM is practically implemented by means of complex and bulky devices, operated by trained personnel, that incorporate laser-based radars (Lidars) or Visual-SLAM (V-SLAM) cameras [13], [14], [15], [16], [17]. Unfortunately, these devices are not only expensive and power-hungry,

but also require perfect visibility and must be operated manually, so they are not suitable for incorporation into mobile devices meant to explore the environment automatically.

In this regard, a methodological and technological shift was proposed in [18], [19] to tackle the SLAM problem by introducing the *personal radar* concept, which concerns the adoption of R-SLAM techniques in handheld devices. Indeed, taking advantage of the fact that evolutionary 5G and beyond-5G scenarios envisage the integration of quasi-pencil beam antennas at mm-wave and THz bands, it is possible to consider utilizing the same hardware for implementing (personal) radar functionalities, overcoming the limitations of Lidar-based and Visual-based SLAM and taking a significant step in the direction of the “integrated communication and sensing” [20] paradigm.

According to the *personal radar* concept, it is thus envisioned that mobile devices will be able to accurately scan the environment by transmitting probe radio signals via the generation of narrow radio beams pointing in different directions (beamsteering), and by receiving the signal reflected by the surroundings [19]. Processing such radio echoes will allow the mobile device to retrieve ranging and bearing information, and will make it possible to derive the maps of indoor spaces [12], [21], [22]. Jointly with the generation of the map, the self-localization of the device within the physical environment is also carried out by the *personal radar*, which thus turns into an infrastructure-free, zero-cost, non-intrusive, and accurate indoor localization system based on R-SLAM techniques, eliminating the need for additional infrastructure.

So far, state-of-the-art SLAM algorithms have been primarily designed for Lidars, which generate a one-dimensional representation of the environment for each complete scan (i.e., after exploring all angular directions). Specifically, a scan vector is produced, containing only the distance (i.e., the range) from the laser source of a single object, if present, in each angular direction. Contrarily, radar measurements are characterized by a richer information content than those of Lidars. In fact, for each complete scan, radars generate a *two-dimensional* representation of the environment, namely, the range-angle matrix, which can ultimately be meant as an image of the surrounding scenario. Indeed, considering the high range-angle resolution expected from THz radars, radio images are anticipated to provide a fairly accurate representation of the surrounding environment. This creates an opportunity to utilize algorithms typically designed for image processing, such as those based on Fourier-Mellin transforms [23], [24], for R-SLAM purposes. These algorithms, with appropriate adjustments, are expected to better leverage the complete information contained in radar images compared to algorithms that operate on one-dimensional scan vectors, such as the widely-used laser Scan Matching algorithm [25].

Along this direction, in this article we first introduce a Fourier-Mellin-based approach for joint localization and mapping using radio signals in the THz frequency range, also proposing an ad-hoc simplified version tailored for portable devices, where low complexity is an important requirement. Then, the performance of the proposed schemes is assessed using real-world THz radar measurements and is compared with state-of-the-art SLAM techniques, demonstrating the superiority of the

proposed approaches. To fully understand the THz backscattering phenomenon, we also provide an experimental characterization of the THz backscattering channel using the same radar.

#### A. Related Works and Proposed Contribution

Surveys on the general SLAM problem can be found in [11], [13], which provide an overview of various techniques, including FastSLAM, GraphSLAM, and belief propagation SLAM [15], [26], [27], [28]. Initially, R-SLAM was predominantly employed in radar and automotive niche applications [29], [30], [31]. For instance, in [29], an algorithm utilizing the iterative closest point (ICP) graph method is presented, which matches consecutive scans obtained from a frequency-modulated continuous-wave (FMCW) radar along with odometry information. It exhibits a mean translational error as low as 0.62 m using a real-world dataset at millimeter waves collected in large outdoor areas. A similar graph-based approach is used in [31] to perform outdoor SLAM under diverse weather conditions.

As already pointed out, R-SLAM has recently attracted a lot of interest for its utilization in current and next-generation wireless systems for mobile personal applications. In fact, the literature features several works on SLAM that employ RF signals, including those employed by WiFi, Bluetooth, and LTE technologies. For example, in [32], the authors propose an approach that combines multiple sources of RF signals, such as WiFi, Bluetooth, and 4G LTE, to construct signal or radio maps. Conversely, [33], [34], [35] investigate the utilization of 5G and mmWave technologies for SLAM applications, aiming to localize the mobile user and determine the positions of signal sources. In [36] a full duplex radio/radar technology is proposed for joint communication and sensing. A method based on fingerprinting can be found in [37], whereas the authors in [38], [39] discuss the possibility to realize R-SLAM-like applications with large intelligent surfaces.

We would like to point out that the common denominator in prior literature on R-SLAM using RF signals, like 5G, is not to localize the user and construct a topological map of the environment (as we do in this article). Instead, the main focus has been on localizing the user and determining the positions of signal sources (e.g., base stations), or achieving user localization using a single anchor node by exploiting the multipath. The prevailing approach adopted by the majority of studies is to perform R-SLAM by employing Bayesian filtering approaches to detect and track the dominant multipath components [33], [40], [41], [42], [43], [44].

Attempts to merge typical image processing approaches with R-SLAM in the microwave band can be found in [30], where the Fourier-Mellin transform is used to register consecutive radar images obtained through an FMCW technology within an EKF-SLAM framework, and in [45], where the scale-invariant feature transform (SIFT) is adopted to extract trackable features from radar images which are subsequently matched with features from laser scans.

To further improve angular and range precision, THz technology has been mainly investigated for imaging [46], [47], and rarely for localization [48], but only separately. Recently,

a R-SLAM system for indoor flying agents at THz has been investigated in [49] which relies on the deployment of passive tags and a synthetic aperture radar capable of millimeter-level localization accuracy. To the authors' knowledge, R-SLAM exploiting the imaging potential at THz has yet to be explored and validated experimentally.

Considering the limitations of the current literature on THz R-SLAM, the main contributions of our work can be summarized as follows.

- We develop an ad-hoc pre-processing scheme, including ghost-effect mitigation (GEM) and noise-masking (NM) strategies, to reduce the presence of outliers and artifacts that might appear in radar measurements, thus selecting the most informative range-angle information to be provided to the R-SLAM algorithm.
- We propose a novel R-SLAM algorithm based on the Fourier-Mellin transform, commonly employed in image processing, that accounts for the specific observation model associated with THz radars. A simplified version of the previous algorithm is also introduced, involving less computational complexity and thus facilitating its integration into personal devices.
- We provide a joint delay and angular characterization of the backscattering THz channel through an extensive measurement campaign carried out in an indoor environment. To the best of authors' knowledge, even if sub-THz and THz 1-way channels have already been modelled for communication purposes [50], [51], [52] and THz backscattering measurements have been recently performed in bistatic configurations [53], the literature still lacks a characterization and understanding of the THz backscattering channel in a quasi-monostatic configuration for R-SLAM-based applications.
- Finally, the performance of the proposed R-SLAM schemes is compared with the state-of-the-art SLAM approach for Lidar measurements, namely the *Laser Scan Matching* algorithm [25]. It is worth noting that, to the authors' knowledge, no article provides such a comparison with experimental data at THz. Based on real-world radar measurements, the numerical results show the potential for achieving infrastructure-less indoor localization and mapping using radio-based techniques in the THz frequency range, offering accuracy at the centimeter level and even down to millimeter-level precision.

This article extends our previous works [18], [19], [54], which focused solely on mapping and targeted systems operating at millimeter waves. In this study, we take a step further by investigating the localization aspect and delving into operations within the THz frequency band, also providing experimental results to support our findings.

The rest of the article is organized as follows: Section III introduces the R-SLAM problem, and radar-signal pre-processing schemes including mapping; Section IV describes the relative pose estimation algorithms considered and proposed in this article; Section V illustrates the measurement campaigns and the delay–angular channel characterization; Section VI discusses

the performance of the proposed R-SLAM algorithms; and Section VII draws the conclusions.<sup>1</sup>

## B. Notation

Boldface lower-case letters are vectors (e.g.,  $\mathbf{x}$ ). In contrast, boldface capital letters are matrices (e.g.,  $\mathbf{A}$ ),  $\mathbf{I}_N$  and  $\mathbf{0}_N$  are respectively the identity and zero matrices of size  $N \times N$ , while  $\mathbf{0}_{M \times N}$  is the zero matrix of size  $M \times N$ . The notation  $a_{n,m} = [\mathbf{A}]_{n,m}$  represents the  $(n, m)$ th element of matrix  $\mathbf{A}$ .  $(\cdot)^T$  and  $(\cdot)^*$  indicate the transpose and complex conjugate operators, respectively.

## II. MOVING FROM MM-WAVE R-SLAM TO THz R-SLAM: ADVANTAGES, DISADVANTAGES, AND CHALLENGES

Transitioning from mmWave R-SLAM to THz R-SLAM entails certain trade-offs. On the one hand, THz R-SLAM suffers from increased path loss, signal blockage, and reduced transmission power, which may constrain its operating range compared to mmWave R-SLAM. Moreover, THz technology is still in its early stages of development, with significant challenges such as the realization of low phase-noise oscillators, efficient power amplifiers, and compact MIMO antennas capable of electronic beamsteering. [55], [56].

On the other hand, however, THz R-SLAM can leverage larger bandwidths to increase spatial accuracy and highly directive antennas with low sidelobes to achieve improved angular resolution and reduce the occurrence of artifacts. Moreover, operating in the THz frequency range opens up new opportunities, as the increased precision of THz radars generates fairly accurate radio images of the environment. This, in turn, allows for the adoption of algorithms, originally conceived for image processing, that can be conveniently adopted for R-SLAM purposes.

It should also be remarked that at mmWave frequencies, reflections from obstacles are predominantly specular in nature. This implies that when a radar signal encounters an obstacle at a high incident angle, it may not be reflected back towards the radar, causing the object to appear transparent. Conversely, at THz frequencies, reflections from obstacles exhibit a predominantly diffuse nature because the wavelength becomes comparable to the roughness of typical materials, whereby the electromagnetic wave scatters in a multitude of directions, thus enhancing the probability of detecting an obstacle even at significant incident angles. These distinct propagation characteristics have a significant impact on the design of SLAM algorithms and their robustness to artifacts.

## III. THz RADIO SLAM

In this section, we introduce the proposed R-SLAM approach tailored to a mobile device offering THz-based radar functionalities. We first formalize the problem statement and then describe

<sup>1</sup>Part of the content of this manuscript appeared in our conference article [21], which, however, did not include the original R-SLAM algorithms introduced in this manuscript nor the different scenarios considered here for their experimental validation. This article also proposes additional results from the backscattering channel characterization campaign.

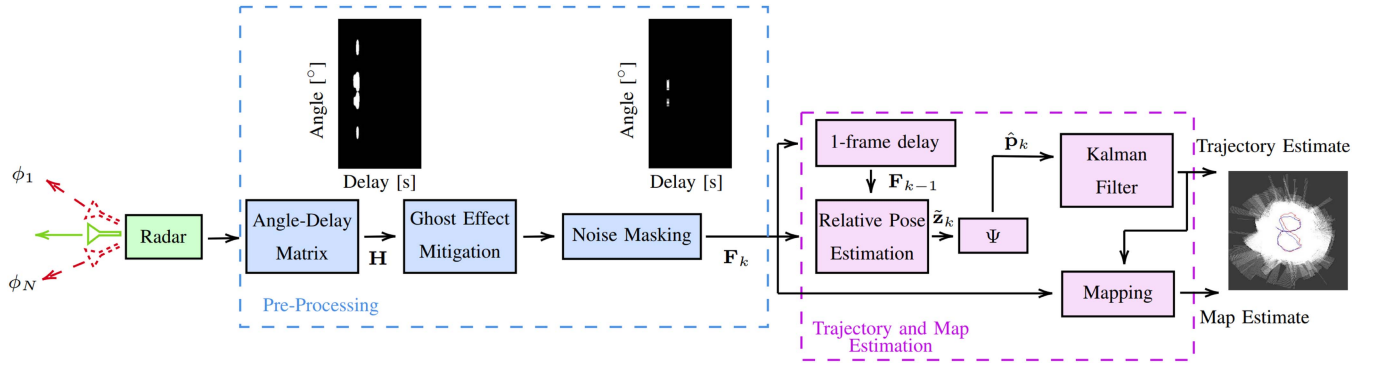


Fig. 1. R-SLAM: Proposed processing chain. We denoted with  $\Psi$  the operations of (12)–(14) that transform the relative pose  $\tilde{\mathbf{z}}_k = [\tilde{d}_x, \tilde{d}_y, \tilde{d}\theta]^T$  on the absolute pose  $\hat{\mathbf{p}}_k$ . Possible implementations of the “Pose Estimation” block are depicted in Figs. 3–4.

the processing chain that, starting with raw radar measurements, leads to the estimation of the user’s trajectory and the automatic mapping of the environment.

#### A. Problem Statement

We consider a 2D scenario in which the state of a mobile user at the (discrete) time instant  $k$ , with time step  $T_F$ , is denoted by

$$\mathbf{x}_k = [x_k, y_k, \dot{x}_k, \dot{y}_k, \theta_k, \dot{\theta}_k]^T \quad (1)$$

which accounts for the user’s position coordinates  $(x_k, y_k)$ , orientation  $\theta_k$  and their variation speeds  $(\dot{x}_k, \dot{y}_k)$  and  $\dot{\theta}_k$ , respectively. Moreover, we denote by

$$\mathbf{p}_k = [x_k, y_k, \theta_k,]^T \quad (2)$$

the absolute pose of the user.

Our objective is to devise a processing chain that, starting from raw measurements provided by the THz radar, is capable of estimating in real-time the trajectory of the mobile user up to time  $k$ , i.e., the sequence of states  $\mathbf{x}_{[1:k]}$  (and therefore of poses  $\mathbf{p}_{[1:k]}$ ), as well as the map of the surrounding environment.

Classical solutions to the joint localization and mapping problem are typically found in the realm of SLAM algorithms, which have been extensively explored in the literature in the context of laser-based measurement sources. In our case, however, the final objective must be achieved starting from radio measurements, which requires ad hoc strategies that fall within the far less investigated R-SLAM field.

#### B. Pre-Processing of Radar Signals

Radio signals backscattered by the environment have to be properly processed in order to infer the map of the scenario and, simultaneously, track the position of the user. In the following, we will discuss each step of the processing chain, which is depicted in Fig. 1. In order to keep our discussion general, we will not focus on a particular radar technology, but rather we suppose that the radar equipment provides the sampled channel impulse responses (CIRs) of the two-way channel for a set  $\{\phi_1, \phi_2, \dots, \phi_N\}$  of  $N$  angular directions. These can be obtained, for example, using a MIMO radar where the signal emitted by the transmitting antennas and backscattered by the

environment is collected by an array of receiving antennas [57]. Such outcomes are then processed as described below. How the sampled CIRs were obtained through measurements made in a real environment in the 300 GHz band will be explained in Section V.

1) *Generation of the Angle-Delay Matrix:* As mentioned above, let us assume that the radar sounder outputs  $M$  samples, with sampling time  $T_s$  (time resolution), of the backscatter CIR for  $N$  different angles of view  $\phi_n$  uniformly distributed in the range  $[-90^\circ, 90^\circ]$ . The magnitudes of these samples are gathered into the *Angle-Delay* matrix

$$\mathbf{H} = \{|h_{n,m}|\}, \quad n = 1, 2, \dots, N, \quad m = 1, 2, \dots, M \quad (3)$$

so that the  $n$ th row of  $\mathbf{H}$  contains the magnitudes of  $M$  (noisy) samples of the CIR in the angular direction  $\phi_n$ . In particular, for a given angular direction  $\phi_n$ ,  $|h_{n,m}|$  refers to the time instant  $t_m = T_{\min} + (m - 1)T_s$ ,  $m = 1, 2, \dots, M$ , with  $T_{\min}$  denoting the minimum two-way propagation delay which is considered to remove the contribution of the direct coupling between the transmitting and receiving antennas of the radar. Clearly, by converting propagation delays into distances between the radar and the reflecting objects, the generic element  $|h_{n,m}|$  corresponds to a range  $d_m = d_{\min} + (m - 1)d$  in the angular direction  $\phi_n$ , where  $d_{\min} = cT_{\min}/2$  is the minimum detection distance,  $d = cT_s/2$ , and  $c$  is the speed of light.

2) *Ghost Effect Mitigation:* Ideally, an antenna oriented in a given direction should only receive signals coming from the same direction, i.e., reflected from objects intercepted by the antenna axis. This property is a peculiar feature of Lidars because of the extremely narrow laser beam. Unfortunately, even though very narrow beams can be realized at THz frequencies, unwanted sidelobes of the antenna’s radiation pattern might catch also echoes coming from other directions, then making R-SLAM much more challenging than classical Lidar-based SLAM. In fact, the radar might erroneously infer the presence of an object in the direction where the main beam of the antenna is oriented due to echoes coming from other directions, thus showing ghost artifacts [58].

As shown in Fig. 1, to mitigate this phenomenon a ghost-effect mitigation (GEM) procedure is performed, which operates on each column  $\mathbf{h}_m$  of  $\mathbf{H}$ , with  $m = 1, 2, \dots, M$ . In particular, for

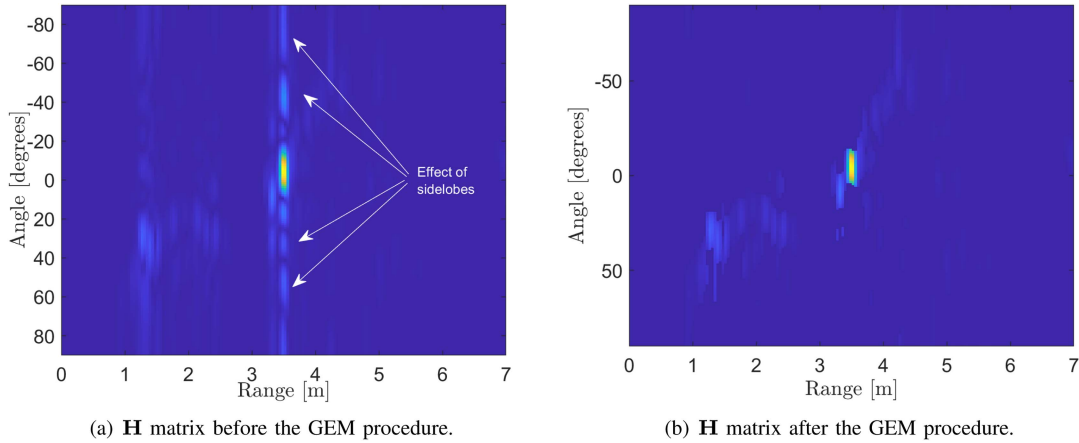


Fig. 2. Impact of the GEM procedure. Single obstacle located at three meters in front of the radar working at 77 GHz with  $\eta_{CL} = 0.4$ .

each column vector

$$\mathbf{h}_m = [|h_{1,m}|, |h_{2,m}|, \dots, |h_{n,m}|, \dots, |h_{N,m}|]^T \quad (4)$$

of  $\mathbf{H}$  (that is, for each distance from the radar), the maximum value is determined as

$$\hat{h}_m = \max(\mathbf{h}_m) \quad (5)$$

where  $\hat{h}_m$  corresponds to the strongest echo detected at the considered distance. Then, we define a threshold

$$\xi_m^{(GEM)} = \eta_{CL} \cdot \hat{h}_m, \quad 0 < \eta_{CL} \leq 1 \quad (6)$$

such that, for each column vector  $\mathbf{h}_m$ , we operate as follows

$$|h_{n,m}| = \begin{cases} |h_{n,m}| & \text{if } |h_{n,m}| \geq \xi_m^{(GEM)} \\ 0 & \text{if } |h_{n,m}| < \xi_m^{(GEM)} \end{cases} \quad (7)$$

In other words, by properly defining the parameter  $\eta_{CL}$ , which depends on the sidelobes level, and hence, on the antenna radiation pattern, it is possible to mitigate the presence of artifacts. The rationale behind the GEM method proposed is that it is unlikely that multiple obstacles are present exactly at the same distance from the radar, whereas echoes captured by sidelobes appear exactly at the same distance. Fig. 2 shows an example of the beneficial impact of the GEM algorithm on a matrix  $\mathbf{H}$  obtained from measurements taken in the 77 GHz band. Although in this article we operate with measurements taken in the [235 – 320] GHz band, we purposely switched to the 77 GHz band for the purpose of generating Fig. 2 to better highlight the ghost artifact phenomenon, which is visually more evident in the millimeter-wave band because of the lower resolution of the radar.

3) *Noise Masking*: Another important impairment affecting the accuracy of measurements is the background noise, either received by the antenna or generated by the radar circuitry itself. Radars usually mitigate its impact by running a NM algorithm that eliminates all the signal components that fall below a certain masking threshold. In our case, the NM algorithm operates as follows. First, it detects the peak of the matrix  $\mathbf{H}$ , that is,

$$h_{\max} = \max(\mathbf{H}). \quad (8)$$

Then, similarly to the GEM algorithm, it requires to define the threshold

$$\xi^{(NM)} = \eta_{CF} \cdot h_{\max}, \quad 0 < \eta_{CF} \leq 1 \quad (9)$$

where  $\eta_{CF}$  is a properly chosen parameter that depends on the background noise and it can be based, for instance, on the constant false alarm rate (CFAR) strategy [57]. Given this threshold, the matrix  $\mathbf{H}$  is cleaned of the unwanted noise contribution as follows

$$|h_{n,m}| = \begin{cases} |h_{n,m}| & \text{if } |h_{n,m}| \geq \xi^{(NM)} \\ 0 & \text{if } |h_{n,m}| < \xi^{(NM)} \end{cases} \quad (10)$$

As shown in Fig. 1, after undergoing the GEM and NM processes, the response to matrix  $\mathbf{H}$  is denoted as  $\mathbf{F}_k$  and is referred to as *frame*. The subscript  $k$  has been introduced to emphasize that a new frame is generated each time the radar performs a complete scan of the environment, which occurs at time instants  $k T_F$ . As evident in Fig. 1, as soon as a new frame  $\mathbf{F}_k$  is generated, it is passed to the subsequent stage, which is in charge of updating the estimates of the mobile user's trajectory and of the environment map.

### C. User's Trajectory Estimation

As shown in Fig. 1, the estimation of the user's trajectory is performed by means of a Kalman filter on the basis of the pose estimates  $\hat{\mathbf{p}}_k$  obtained by comparing the current frame  $\mathbf{F}_k$  with that of the previous time instant,  $\mathbf{F}_{k-1}$ . In this regard, it is worth emphasizing that  $\mathbf{F}_k$  and  $\mathbf{F}_{k-1}$  are two-dimensional representations of the scanned area (in polar coordinates), hence they can be meant as “radar images” of the sensed environment in successive instants. This suggested us to derive the pose estimates by means of algorithms that were initially conceived for image processing.

The specific pose estimation algorithms considered in this manuscript, which represent one of the major contributions of our work, deserve detailed descriptions, which are therefore provided in the specially dedicated Section IV. In any case, whatever pose estimation algorithm is adopted,  $\hat{\mathbf{p}}_k$  is derived

starting from the estimated relative pose vector

$$\tilde{\mathbf{z}}_k = [\tilde{d}x, \tilde{d}y, \tilde{d}\theta]^T \quad (11)$$

whose elements are the estimated horizontal shift, vertical shift, and rotation of the current pose with respect to the previous one, all referenced to the radar-based coordinate system, as well as a quality indicator  $q \in [0, 1]$  of the estimates. It should be emphasized that  $\tilde{\mathbf{z}}_k$  refers to the local coordinate system of the mobile user, i.e., the radar point of view, therefore it has to be transformed into the absolute coordinate system by considering the latest available estimate of the mobile user's rotation  $\hat{\theta}_{k-1}$ , that is,

$$\mathbf{z}_k = \mathbf{U}(\hat{\theta}_{k-1}) \tilde{\mathbf{z}}_k \quad (12)$$

where

$$\mathbf{U}(\theta) = \begin{bmatrix} \cos \theta & \sin \theta & 0 \\ -\sin \theta & \cos \theta & 0 \\ 0 & 0 & 1 \end{bmatrix} \quad (13)$$

denotes the rotation matrix of angle  $\theta$ . Given  $\mathbf{z}_k$ , and the previous absolute pose estimate, denoted by  $\hat{\mathbf{p}}_{k-1} = [\hat{x}_{k-1}, \hat{y}_{k-1}, \hat{\theta}_{k-1}]^T$ , the current raw absolute pose estimate is

$$\hat{\mathbf{p}}_k = \hat{\mathbf{p}}_{k-1} + \mathbf{z}_k. \quad (14)$$

The processing steps outlined in (12), (13), and (14) are represented in Fig. 1 by the block labelled  $\Psi$ , which receiving as input  $\tilde{\mathbf{z}}_k$  generates as output  $\hat{\mathbf{p}}_k$ . The latter is then passed to the Kalman filter, which is in charge of the trajectory estimation accounting for the user's mobility model and the quality of the relative pose estimates. In this regard, we point out that when it comes to tracking algorithms, it is customary to consider a Markovian state-space model to describe the evolution of the state, which is based on the following second-order kinematic linear model [59], [60]

$$\mathbf{x}_{k+1} = \mathbf{A} \mathbf{x}_k + \mathbf{w}_k \quad (15)$$

where

$$\mathbf{A} = \begin{bmatrix} \mathbf{I}_2 & T_F \mathbf{I}_2 & \mathbf{0}_2 \\ \mathbf{0}_2 & \mathbf{I}_2 & \mathbf{0}_2 \\ \mathbf{0}_2 & \mathbf{0}_2 & \tilde{\mathbf{A}} \end{bmatrix} \quad (16)$$

is the transition matrix and  $\mathbf{w}_k \sim \mathcal{N}(\mathbf{0}_{1 \times 6}; \mathbf{Q})$  is the process noise whose covariance matrix  $\mathbf{Q}$  is [60]

$$\mathbf{Q} = \begin{bmatrix} w_0 \frac{T_F^3}{3} \mathbf{I}_2 & w_0 \frac{T_F^2}{2} \mathbf{I}_2 & \mathbf{0}_2 \\ w_0 \frac{T_F^2}{2} \mathbf{I}_2 & w_0 T_F \mathbf{I}_2 & \mathbf{0}_2 \\ \mathbf{0}_2 & \mathbf{0}_2 & \tilde{\mathbf{Q}} \end{bmatrix} \quad (17)$$

with  $\mathbf{I}_N$  and  $\mathbf{0}_N$  being respectively  $N \times N$  identity and zero matrices,  $w_0$  being the power spectral density of the linear acceleration noise, and with

$$\tilde{\mathbf{A}} = \begin{bmatrix} 1 & T_F \\ 0 & 1 \end{bmatrix}, \quad \tilde{\mathbf{Q}} = \begin{bmatrix} \omega_\theta \frac{T_F^3}{3} & \omega_\theta \frac{T_F^2}{2} \\ \omega_\theta \frac{T_F^2}{2} & \omega_\theta T_F \end{bmatrix} \quad (18)$$

where  $w_\theta$  is the power spectral density of the angular acceleration noise (process noise), which depends on the expected mobility of the user [60].

The evolution of the absolute state  $\mathbf{x}_k$  can be tracked by means of a Kalman filter, fed step-by-step with the current raw absolute pose estimate,  $\hat{\mathbf{p}}_k$ , using the following observation model

$$\hat{\mathbf{p}}_k = \mathbf{B} \mathbf{x}_k + \boldsymbol{\nu}_k \quad (19)$$

where

$$\mathbf{B} = \begin{bmatrix} 1 & 0 & 0 & 0 & 0 & 0 \\ 0 & 1 & 0 & 0 & 0 & 0 \\ 0 & 0 & 0 & 0 & 1 & 0 \end{bmatrix} \quad (20)$$

and  $\boldsymbol{\nu}_k \sim \mathcal{N}(\mathbf{0}_3; \mathbf{R})$  is the estimation noise modelled as Gaussian random vector with covariance matrix [60]

$$\mathbf{R} = \text{diag}(\sigma_x^2/q^2, \sigma_y^2/q^2, \sigma_\theta^2/q^2) \quad (21)$$

that accounts for the reliability  $q$  of the current relative pose estimate, generated as will be explained in Section IV, being  $\sigma_x^2 = \sigma_y^2$ , and  $\sigma_\theta^2$  the estimation noise power expected by the specific relative pose estimator. At each time instant  $k$ , the Kalman filter provides an estimate  $\hat{\mathbf{x}}_k$  of the state  $\mathbf{x}_k$  as well as its covariance matrix.

#### D. Automatic Mapping

Concerning the mapping task, in this article we employ an *occupancy grid* approach to represent the indoor environment [61]. This approach involves dividing the scenario into a fine grid of cells and solving the problem of determining the occupancy probability of each cell by utilizing measurements and estimated trajectories. In particular, for each cell, the likelihood of its occupancy must be calculated on the basis of the collected observations.

According to [18], the actual map at time instant  $k$  can be represented as a vector of cells as<sup>2</sup>

$$\mathbf{m}_k \triangleq [m_{1,k}, \dots, m_{i,k}, \dots, m_{N_{\text{cell}},k}]^T \in \mathbb{B}^{N_{\text{cell}}} \quad (22)$$

where  $m_{i,k} \in \mathbb{B}$  represents the true occupancy of the  $i$ -th cell ( $m_{i,k} = 0$  denotes an empty cell, whereas  $m_{i,k} = 1$  denotes an occupied cell),  $\mathbb{B}$  is the Boolean domain, and  $N_{\text{cell}}$  is the total number of considered cells. In the sequel, we consider a stationary map, that is  $\mathbf{m}_k = \mathbf{m}, \forall k$ .

The goal of the mapping algorithm is to infer (22) by computing the maximum of the *a-posteriori* probability mass function (*belief*) given the history of frame observations and the estimated trajectories (see Fig. 1). Denoting with  $b_k(m_i)$  the belief of occupancy of the  $i$ -th cell at time instant  $k$ , the following steps are performed:

- *Initialization*: If no prior map information is available, a possible initialization is  $b_0(m_i) = 0.5$ , corresponding to a complete uncertainty,  $\forall i = 1, 2, \dots, N_{\text{cell}}$ .
- *Scan vector generation*: The cleaned Angle-Range matrix  $\mathbf{F}_k$ , which is obtained as the output of the GEM and NM processing at the time instant  $k$ , is passed to the mapping algorithm (the Mapping block in Fig. 1), whose first task is to generate a 1-by- $N$  vector of ranges  $\mathbf{v}_k$  similar to the one provided by a Lidar scan. Specifically,  $\mathbf{v}_k$  contains only one

<sup>2</sup>The map might be time-varying due to moving obstacles, such humans or mobile furniture (e.g., chairs).

range value of the current *frame*  $\mathbf{F}_k$  for each considered steering angle, i.e.,  $\mathbf{v}_k = [v_1^{(k)}, v_2^{(k)}, \dots, v_N^{(k)}]$ , with  $v_n^{(k)}$  being the range of the object (if any) seen at the angle  $\phi_n$  by the radar. This result is achieved by comparing each row of the current frame, i.e.,  $\mathbf{f}_n = [|h_{n,1}|, |h_{n,2}|, \dots, |h_{n,M}|]$  of  $\mathbf{F}_k$ , with a suitable threshold  $0 < \eta_{SV} \leq 1$ . The distance corresponding to the first element which exceeds  $\eta_{SV} \cdot f_{\max}$ , with  $f_{\max}$  being the maximum value in  $\mathbf{f}_n$ , is saved in  $\mathbf{v}_k$ .

Similarly, the angles  $\phi_n$  are collected into the angle vector  $\phi = [\phi_1, \phi_2, \dots, \phi_N]$ . The final scan vector at time instant  $k$  is given by  $\mathbf{s}_k = [\mathbf{v}_k^T, \phi^T]$ .

- *Log-Odd Update*: Starting from  $\mathbf{s}_k$ , the beliefs are updated following a classic occupancy grid algorithm [61]. To avoid numerical instability during calculations, a practical solution is to map the belief into the log-odd quantity

$$\ell_k(m_i) \triangleq \log \left( \frac{b_k(m_i)}{1 - b_k(m_i)} \right), \quad \forall i = 1, 2, \dots, N_{\text{cell}}. \quad (23)$$

Since the belief can be expressed as in [60, Eq. 12], and by embedding all the prior information into the term  $\ell_{k-1}(m_i)$ , (23) becomes:

$$\ell_k(m_i) = \log \left( \frac{p(\mathbf{s}_k | m_i = 1)}{p(\mathbf{s}_k | m_i = 0)} \right) + \ell_{k-1}(m_i) \quad \forall i = 1, \dots, N_{\text{cell}} \quad (24)$$

where  $p(\mathbf{s}_k | m_i = 1)$  ( $p(\mathbf{s}_k | m_i = 0)$ ) is the likelihood function considering the current scan  $\mathbf{s}_k$  given the presence of an occupied (empty) cell in  $m_i$ . In our case,  $p(\mathbf{s}_k | m_i = 1)$  can take two values, that is 0.9 when the polar coordinates of the  $i$ th cell are present inside the scan vector  $\mathbf{s}_k$ , and 0.1 otherwise. Finally, the likelihood of having an empty cell is simply given by

$$p(\mathbf{s}_k | m_i = 0) = 1 - p(\mathbf{s}_k | m_i = 1). \quad (25)$$

In (24) we assume that each cell is independent of all the others (including adjacent cells) as for laser observations. Nevertheless, inter-cell correlations can be considered in the observation model to further refine the mapping process [54].

As a concluding statement regarding the above-described algorithm, we underline that the resulting map is obtained by considering the complete history of measurements collected from distinct radar positions. By capitalizing on the spatial diversity inherent in measurements obtained from various locations, this approach effectively mitigates potential issues stemming from signal blockage, suboptimal antenna radiation patterns, and low reflective characteristics of objects.

#### IV. RELATIVE POSE ESTIMATION

In this section, we present the details of the algorithms we have considered for estimating the relative pose, specifically referring to the Pose Estimation block in Fig. 1. Firstly, we introduce the *Laser Scan Matching* algorithm [25], commonly adopted in Lidar-based systems, which is considered here as a benchmark. Then, inspired by the possibility of employing

algorithms typically used for image processing, we propose a modified version of the *Fourier-Mellin* algorithm, specifically adapted to operate with signals provided by a THz radar. Finally, we propose a simplified version of the *Fourier-Mellin*-based algorithm that, having lower computational complexity, is better suited for use in portable devices implementing R-SLAM.

*a) Laser Scan Matching Algorithm*: This methodology was conceived for Lidar-based systems and it is here considered as a benchmark [25]. When fed with laser scans, it has been proved to achieve real-time loop closure and 5 cm resolution [25].

According to this algorithm, the user's relative pose in the current instant  $k$ , given by (11), is derived starting from the current and the previous scan vectors  $\mathbf{s}_k$  and  $\mathbf{s}_{k-1}$ , which are compared to estimate the corresponding translation increments  $(\tilde{d}x, \tilde{d}y)$  and rotation increment  $\tilde{d}\theta$  using a grid-based search.<sup>3</sup> Specifically, the *Laser Scan Matching* algorithm converts  $\mathbf{v}_k$ ,  $\mathbf{v}_{k-1}$  and  $\phi$  into probabilistic grids and finds the pose between the two scans by correlating their grids [25]. The interested reader is referred to [62] for additional details on the strategy adopted by the algorithm to speed up the computation.

*b) Fourier-Mellin-based Algorithm*: With the goal of achieving improved performance compared to the *Laser Scan Matching* algorithm, in this article we propose to estimate the relative pose between two consecutive frames  $\mathbf{F}_k$  and  $\mathbf{F}_{k-1}$  by means of the Fourier-Mellin algorithm [23], [24], which is an FFT-based method used to register<sup>4</sup> two different images searching for the optimal match in the frequency domain. In particular, the objective of the algorithm is to decouple the translation and rotation effects in order to facilitate their estimation.

This algorithm, which was designed to operate on Cartesian images, is here applied to consecutive *frames* in polar coordinates, which in fact can be interpreted as "radio images" of the environment. For the sake of clarity, in the following, we will highlight the dependence of the elements of  $\mathbf{F}_k$  on the distance  $\rho$  and the angle  $\theta$  by treating the frame as a two-dimensional function  $\mathbf{F}_k(\theta, \rho)$ . It is worth pointing out, in this regard, that  $\rho$  and  $\theta$  are here meant as continuous variables, in contrast with the corresponding discrete variables  $d_m$  and  $\phi_n$  introduced in Section III. This choice is aimed at simplifying the notation in the following analysis, the discrete version of which was implemented in our test bed.

The algorithm we propose consists of the main steps shown in Figs. 3–4, which are described hereafter.

- *Step 1*: The current and previous frames  $\mathbf{F}_k(\theta, \rho)$  and  $\mathbf{F}_{k-1}(\theta, \rho)$ , which clearly refer to a polar coordinate system, are converted into the corresponding images  $\mathbf{C}_k(x, y)$  and  $\mathbf{C}_{k-1}(x, y)$  in Cartesian coordinates.
- *Step 2*: Given  $\mathbf{C}_k(x, y)$  and  $\mathbf{C}_{k-1}(x, y)$ , the corresponding 2D Fourier transforms  $\mathcal{F}_k(\xi, \eta)$  and  $\mathcal{F}_{k-1}(\xi, \eta)$  are computed. Assuming that  $\mathbf{C}_k(x, y)$  is a perfectly (i.e., not affected by noise and artifacts) rotated and translated

<sup>3</sup>The scan vectors  $\mathbf{s}_k$  and  $\mathbf{s}_{k-1}$  on which the *Laser Scan Matching* algorithm operates are derived as explained in Section III-D

<sup>4</sup>Image registration is an image processing technique used to align multiple scenes into a single integrated image, compensating rotations, translations and different scaling.

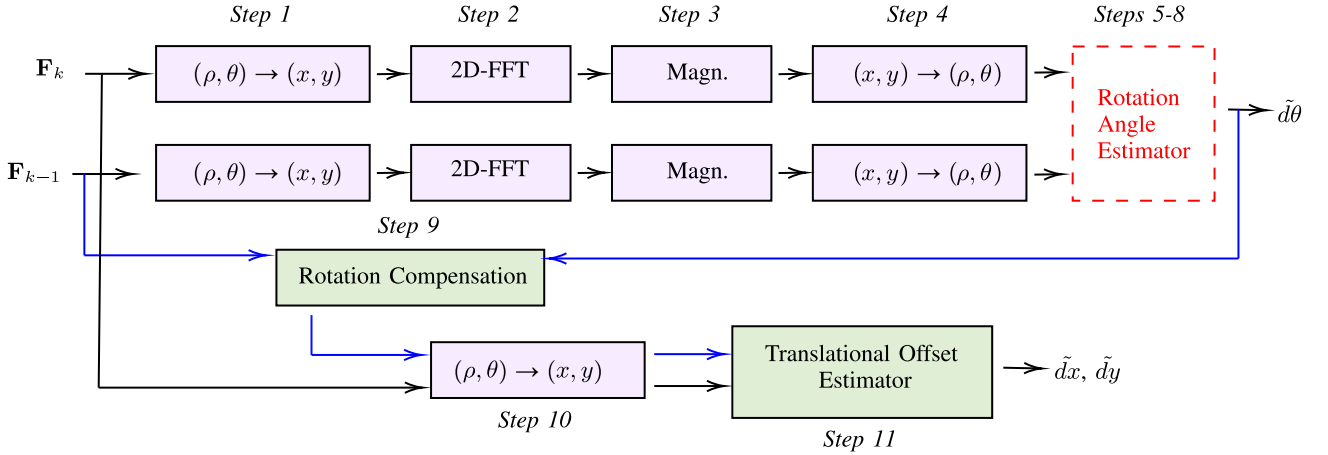


Fig. 3. Relative pose estimation implemented using the Fourier-Mellin-based algorithm. The output is the relative pose  $\tilde{\mathbf{z}}_k = [\tilde{d}x, \tilde{d}y, \tilde{d}\theta]^T$ . The details of the “Rotation Angle Estimator” are depicted in Fig. 4.

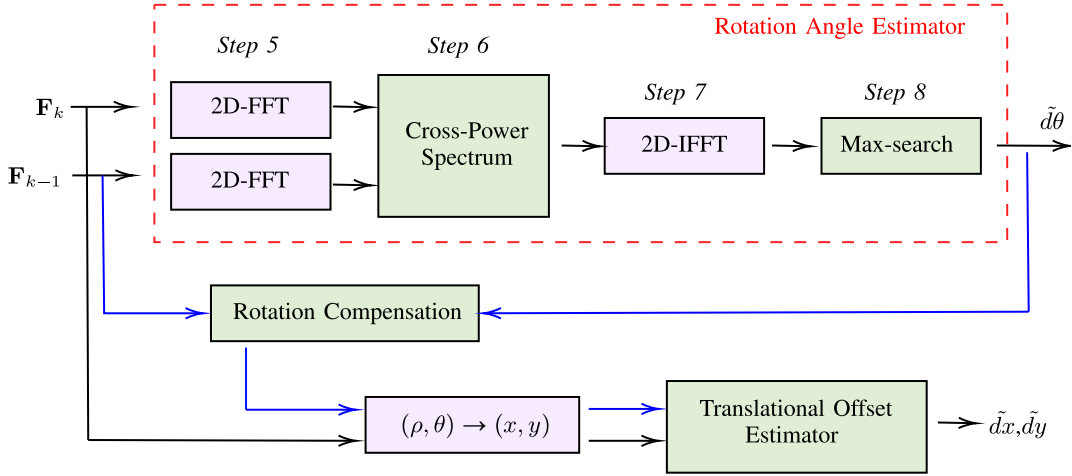


Fig. 4. Relative pose estimation implemented using the simplified Fourier-Mellin algorithm. The output is the relative pose  $\tilde{\mathbf{z}}_k = [\tilde{d}x, \tilde{d}y, \tilde{d}\theta]^T$ .

replica of  $\mathbf{C}_{k-1}(x, y)$ , that is

$$\begin{aligned} \mathbf{C}_k(x, y) = & \mathbf{C}_{k-1}(x \cos(d\theta) + y \sin(d\theta) - dx, -x \sin(d\theta) \\ & + y \cos(d\theta) - dy) \end{aligned} \quad (26)$$

where  $(dx, dy)$  are the translational offsets and  $d\theta$  is the rotation angle from instant  $k - 1$  to instant  $k$ , the relation between the corresponding 2D Fourier transforms is:

$$\begin{aligned} \mathcal{F}_k(\xi, \eta) = & e^{-j2\pi(\xi dx + \eta dy)} \mathcal{F}_{k-1}(\xi \cos(d\theta) + \eta \sin(d\theta), \\ & -\xi \sin(d\theta) + \eta \cos(d\theta)). \end{aligned} \quad (27)$$

- *Step 3:* Given (27), the relation between the magnitudes of  $\mathcal{F}_k(\xi, \eta)$  and  $\mathcal{F}_{k-1}(\xi, \eta)$  is

$$\begin{aligned} \mathbf{M}_k(\xi, \eta) = & \mathbf{M}_{k-1}(\xi \cos(d\theta) + \eta \sin(d\theta), \\ & -\xi \sin(d\theta) + \eta \cos(d\theta)). \end{aligned} \quad (28)$$

From (28) one can argue that the magnitude is translation invariant, as it does not depend on  $(dx, dy)$ . It turns out, therefore, that possible differences between  $\mathbf{M}_k(\xi, \eta)$  and

$\mathbf{M}_{k-1}(\xi, \eta)$  are found to be solely dependent on the rotation  $d\theta$ .

- *Step 4:* By expressing (28) in polar coordinates, it immediately results

$$\mathbf{M}_k(\theta, \rho) = \mathbf{M}_{k-1}(\theta - d\theta, \rho) \quad (29)$$

that represents a convenient formulation for the derivation of the rotation angle  $d\theta$ . Actually, converting the magnitudes from Cartesian to polar coordinates makes it possible to represent rotations as translations in the angular domain, as evident in (29), thus allowing to exploit the translation property of the Fourier transform, as explained in Step 5.

- *Step 5:* By denoting  $\mathcal{M}_k(\mu, \nu)$  and  $\mathcal{M}_{k-1}(\mu, \nu)$  the 2D Fourier transforms of  $\mathbf{M}_k(\theta, \rho)$  and  $\mathbf{M}_{k-1}(\theta, \rho)$ , respectively, it results

$$\mathcal{M}_k(\mu, \nu) = \mathcal{M}_{k-1}(\mu, \nu) e^{-j2\pi\nu d\theta} \quad (30)$$

that features the nice property of having the rotation angle  $d\theta$  included only in the exponential function, which can be easily isolated, as shown in Step 6.



- *Step 6:* By defining the cross-power spectrum  $\text{CPS}_k(\mu, \nu)$  of  $\mathbf{M}_k(\theta, \rho)$  and  $\mathbf{M}_{k-1}(\theta, \rho)$  as

$$\text{CPS}_k(\mu, \nu) = \frac{\mathcal{M}_k(\mu, \nu) \mathcal{M}_{k-1}^*(\mu, \nu)}{|\mathcal{M}_k(\mu, \nu) \mathcal{M}_{k-1}^*(\mu, \nu)|} \quad (31)$$

it immediately follows

$$\text{CPS}_k(\mu, \nu) = e^{-j2\pi\nu d\theta}. \quad (32)$$

- *Step 7:* Taking the inverse Fourier transform of (32) yields a Dirac  $\delta$ -function centered at  $d\theta$ .
- *Step 8:* Finding the location where the maximum of the inverse Fourier transform occurs, allows to derive an estimation  $\tilde{d}\theta$  of the rotation angle  $d\theta$ . When dealing with less-than-perfect images, the peak amplitude can serve as a quality indicator  $q$  for assessing the accuracy of the relative pose estimation to be used in (21).
- *Step 9:* Given  $\tilde{d}\theta$ , it is now possible to apply such rotation to  $\mathbf{F}_{k-1}(\theta, \rho)$ , thus obtaining  $\hat{\mathbf{F}}_{k-1}(\theta, \rho)$ , which (ideally) is aligned in the angle domain with  $\mathbf{F}_k(\theta, \rho)$ .
- *Step 10:* The angle-compensated  $\hat{\mathbf{F}}_{k-1}(\theta, \rho)$  is then converted from polar to Cartesian coordinates, thus becoming  $\hat{\mathbf{F}}_{k-1}(x, y)$ , in preparation for the comparison with  $\mathbf{F}_k(x, y)$ .
- *Step 11:* After Steps 9 and 10,  $\mathbf{F}_k(x, y)$  is (ideally) a translated replica of  $\hat{\mathbf{F}}_{k-1}(x, y)$ . The estimation  $(\tilde{d}x, \tilde{d}y)$  of the translation offset  $(dx, dy)$  can now be derived following the same procedure adopted to estimate the rotation angle  $d\theta$ , starting from Step 5 to Step 8. To avoid confusing the reader with an overly complicated diagram, these steps have been incorporated into the *Translational Offset Estimator* block of Fig. 3, whose inputs, however, are  $\mathbf{F}_k(x, y)$  and  $\hat{\mathbf{F}}_{k-1}(x, y)$ .

*c) Simplified Fourier-Mellin Algorithm:* Considering that THz R-SLAM is intended as an additional feature for future portable devices, the objective of minimizing computational effort and, subsequently, energy consumption led us to develop a simpler, in principle less accurate, version of the above described Fourier-Mellin-based algorithm. The basic idea of this new version is to make the rotation-angle estimator (see the dashed red box in Fig. 3) work directly on  $\mathbf{F}_k(\theta, \rho)$  and  $\mathbf{F}_{k-1}(\theta, \rho)$ , rather than on the magnitude of their Fourier transforms. This means that the steps from 1 to 4 of the original algorithm are skipped, thus leading to the much simpler block scheme shown in Fig. 4. The assumption that makes the simplified algorithm sufficiently accurate is that, passing from  $\mathbf{F}_{k-1}(\theta, \rho)$  to  $\mathbf{F}_k(\theta, \rho)$ , the impact of translations is much lower than the impact of rotations, so that the *Rotation Angle Estimator* is not significantly affected by translations. This requires that a sufficiently small sampling time  $T_s$  is chosen.

Regarding the complexity of the Fourier-Mellin and simplified Fourier-Mellin algorithms, it mainly depends on the number of FFTs involved. Given that the complexity of each FFT is  $\mathcal{O}(N \log N)$ , where  $N$  represents the data size, the Fourier-Mellin algorithm requires 5 FFT computations for each pose estimation, while the simplified Fourier-Mellin algorithm

requires only 3 FFT computations, resulting in a lower overall complexity for the latter.

Despite its simplicity, the numerical results section will demonstrate that the simplified algorithm exhibits similar, and in some cases better, performance compared to the Fourier-Mellin-based algorithm.

*Remark 1:* The block diagram shown in Fig. 1 includes blocks that are specific to the THz band, as well as others that can also be used in the mmWave range. In particular, the macro-block denoted as *Trajectory and Map Estimation*, which incorporates the Fourier-Mellin algorithm, is specifically designed to leverage the ranging and angular accuracy of THz radars. This is because the Fourier-Mellin algorithm requires a fairly accurate radar image of the environment, which is difficult to obtain with mmWave radars. Contrarily, the blocks labelled as *Ghost Effect Mitigation* and *Noise Masking* could also be used to implement mmWave R-SLAM, provided that their parameters are appropriately adjusted.

*Remark 2:* It is important to highlight that the entire procedure described above relies on the estimation of the impulse response of the backscatter channel, which ultimately consists of the channel state information (CSI). As a result, this approach remains applicable regardless of the waveform utilized or the specific methodology employed to derive the CSI estimate. Indeed, the derivation of the CSI is the basis for most of the (de)modulation schemes proposed for ISAC (e.g., for OFDM).

## V. INDOOR BACKSCATTERING CHARACTERIZATION IN THE THZ BAND

This section provides a comprehensive description of the measurement campaigns carried out at THz frequencies, along with the processing techniques employed. The real-world data collected during these campaigns served as input for the R-SLAM algorithms, whose outcomes are presented in Section VI.

### A. Measurement Set up

To emulate the radar operation, the measurement setup, shown in Fig. 5, was based on a four-ports Vector Network Analyzer (VNA) together with converters in order to cover the [235 – 320] GHz band. We employed two linearly polarized horn antennas with gain  $G_{\text{TX}} = G_{\text{RX}} = 20$  dBi and Half Power Beam Width (HPBW) of  $18^\circ$ . The backscatter channel acquisition was operated in a quasi-monostatic configuration, as the TX and RX were co-located on a linear - angular positioner, which allowed mechanical steering and displacement over a 2-meter-long X-axis. Acquisitions were managed by an external computer, which was connected to both the VNA and the positioner controller using Ethernet cables.

### B. Indoor Measurement Campaigns

Two measurement campaigns were carried out at CEA-Leti in a laboratory/office room (shown in Fig. 6) with a size of  $10.2 \times 8.6$  m<sup>2</sup>. In the first measurement campaign, the radar scanned the laboratory in nine positions along a 2-meter straight path with an X-axis step of 0.25 m. This measurement was

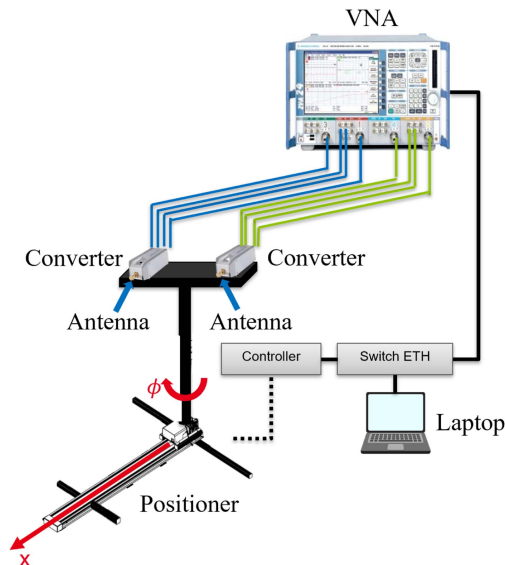


Fig. 5. Measurement setup scheme.

repeated twice, first with the radar pointed towards the direction of movement (Scenario A), then with the radar pointed perpendicular to the direction of movement (Scenario B).

In the second measurement campaign (Scenario C), the radar scanned the environment in 46 positions along an oval path, characterized by diameters of 5 m and 3 m. In the straight segments, the X-axis step size was set at 0.40 m, while in the curved sections, the step sizes varied between 0.23 to 0.27 m to maintain the correlation between the channel responses in adjacent positions.

At each radar location, the positioner rotated the antennas with increments of  $10^\circ$  within the steering range of  $[-90^\circ, 90^\circ]$ . To make it easy to read, the pictures of the three scenarios are reported together with the R-SLAM performance in Section VI. Specifically, the locations where the radar measurements were taken, denoted *positions* in the following, are shown in Figs. 9 (top), 10 (top) and 11 (top), where they appear as red dots.

### C. Generation of the Angle-Delay Matrix

The setup described above emulated a stepped-frequency continuous-waves (SFCWs) radar, with measurements spanning from 235 to 320 GHz and a step size of 10 MHz for each position and steering direction. These measurements yielded the channel frequency responses (CFRs), which were further processed to reduce sidelobe ringing by applying frequency domain filtering. To compute the CIRs, an inverse FFT was performed with a time resolution of  $T_s = 1.56$  ps. For R-SLAM purposes, the CIRs were computed for 181 steering angles  $\phi_n$  at each position using an interpolation process with a step size of  $1^\circ$  within the  $[-90^\circ, 90^\circ]$  range, and then collected to form the Angle-Delay matrix  $\mathbf{H}$ .

### D. Backscattering Channel Characterization

Fig. 7(a) presents an illustrative example of CIRs collected by the radar at position #15 of Scenario C, for 19 steering angles

within the range  $[-90^\circ, 90^\circ]$  and angular step of  $10^\circ$ . These CIRs, which have been normalized by removing the effect of the TX and RX antenna gains, provide valuable insights into the backscatter characteristics of the surrounding environment and, ultimately, its map. For example, still focusing on the measurements collected at position #15 of Scenario C (see Fig. 7(a)), we were able to derive a preliminary (albeit approximate and incomplete) map of the environment by combining the power delay profiles (PDPs) associated with the CIRs collected from all steering directions [63]. This resulted in the creation of the power angular delay profile (PADP) at the considered position, which allowed an estimate of the map to be derived immediately. In this regard, a visual comparison between the PADP obtained at position #15 and the actual locations of the walls is shown in Fig. 7(b). Each point corresponds to a detected path, characterized by a specific delay and arrival angle, with the color indicating the power normalized relative to the highest path power. Notably, the radar echoes detected are consistent with the expected echoes from the primary scatterers in the environment, namely the walls.

Interestingly, a part of the horizontal wall depicted in Fig. 7(b) shows a lack of backscatter response. It is noted, in this regard, that the wall is made of plasterboard, which has poor reflective properties. Additionally, the undetected part of the wall lacks any objects positioned in front of it that could have triggered radar reflections. It is essential to emphasize, however, that the map depicted in Fig. 7(b) was obtained solely from the measurements provided by the radar at position #15. In contrast, the methodology proposed in this article derives the map by considering measurements collected throughout the entire radar path, resulting in significantly improved outcomes. In fact, the numerical results reported in Section VI will show that the entire wall is successfully mapped, thanks to the measurement taken when the radar gets closer to it.

In order to characterize the backscatter channel, it is of interest to investigate the root mean square (RMS) delay and the angular spread of the paths detected after the GEM algorithm.<sup>5</sup> Specifically, for each position within a given scenario (A, B, or C) and considering all the paths collected in the PADP, which accounts for all steering directions, the RMS delay spread is defined as:

$$\tau_{\text{rms}} = \sqrt{\frac{\sum_{k=1}^K (\tau_k - \tau_m)^2 \alpha_k^2}{\sum_{k=1}^K \alpha_k^2}} \quad (33)$$

where  $\tau_m$  is the mean arrival delay defined as

$$\tau_m = \frac{\sum_{k=1}^K \tau_k \alpha_k^2}{\sum_{k=1}^K \alpha_k^2} \quad (34)$$

and  $K$ ,  $\alpha_k^2$ ,  $\tau_k$  are the number of detected paths, the power, and the arrival delay of the  $k$ th path, respectively.

<sup>5</sup>The characterization of the backscatter channel was performed without using the NM algorithm to avoid the elimination of weak paths, which could potentially be present.



Fig. 6. Pictures of the environment.

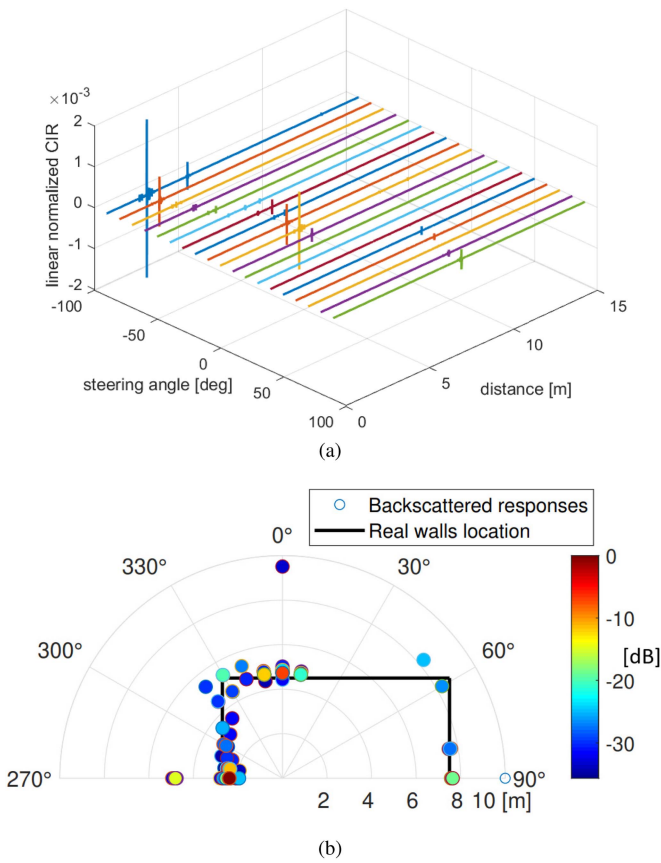


Fig. 7. Normalized CIRs for all steering angles at position #15 of Campaign C (a), with delays mapped into distances; polar representation of the normalized power angular delay profile (PADP) at position #15 of Scenario C compared to the actual map of the environment (b).

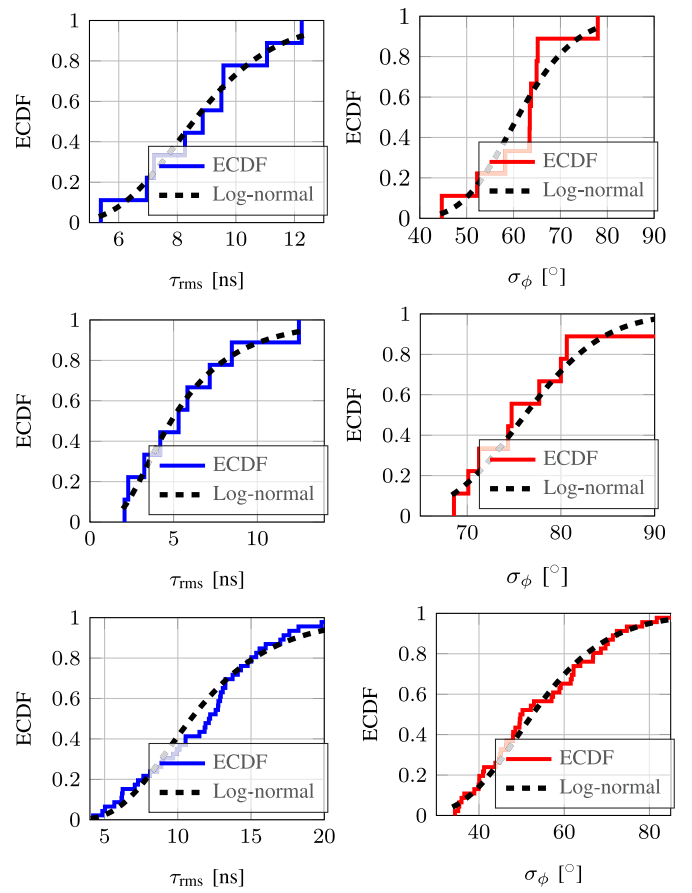


Fig. 8. Empirical CDFs of the delay spread and angular spread for all the positions of Campaign A (top), Campaign B (middle), and Campaign C (bottom).

Similarly, the angular spread can be computed at each position of a scenario using Fleury's definition, as in [64]

$$\sigma_{\phi} = \sqrt{\frac{\sum_{k=1}^K |e^{j\phi_k} - \mu_{\phi}|^2 \alpha_k^2}{\sum_{k=1}^K \alpha_k^2}} \quad (35)$$

where  $\phi_k$  is the arrival angle of the  $k$ th path and  $\mu_{\phi}$  is the mean arrival azimuth defined as

$$\mu_{\phi} = \frac{\sum_{k=1}^K e^{j\phi_k} \alpha_k^2}{\sum_{k=1}^K \alpha_k^2}. \quad (36)$$

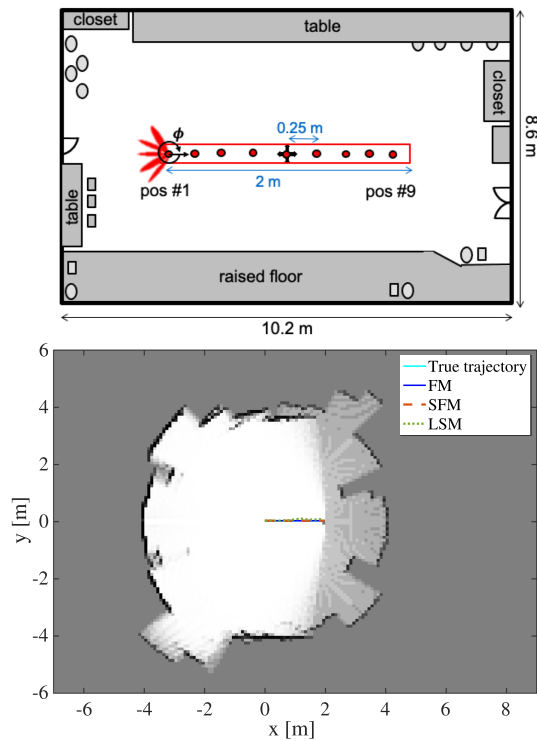


Fig. 9. Measurement Scenario A (top); Estimated trajectories and map (bottom).

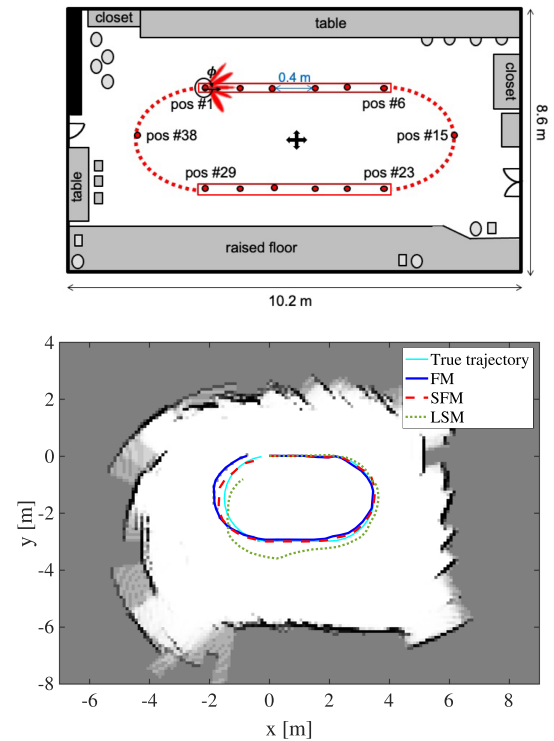


Fig. 11. Measurement Scenario C (top); Estimated trajectories and map (bottom).

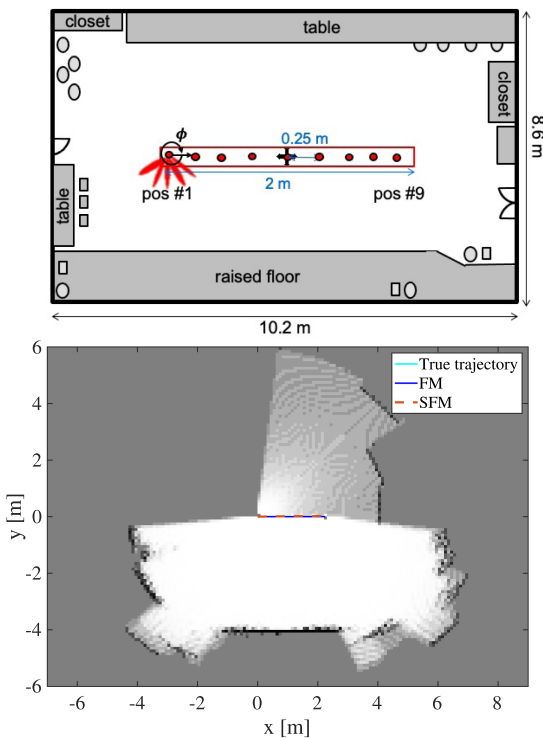


Fig. 10. Measurement Scenario B (top); Estimated trajectories and map (bottom).

Based on the provided definitions, Fig. 8 displays the empirical cumulative distribution functions (ECDFs) of the RMS delay spread and angular spread of the paths detected in each scenario after applying the GEM algorithm. Since these metrics are calculated by considering all positions within each of the three scenarios depicted in Fig. 9 (top), 10 (top), and 11 (top), they provide a characterization of their backscattering channels at THz frequencies. A more concise characterization is provided by the average RMS delay spreads, 8.79 ns, 5.67 ns, and 10.86 ns, and the average angular spreads,  $61.5^\circ$ ,  $76.4^\circ$ , and  $52.6^\circ$ , for scenarios A, B, and C, respectively.

The results highlight substantial variations in delays and angular spreads, which are highly dependent on the radar position and steering angle. Interestingly, these variations can be effectively characterized using a log-normal distribution. Notably, the maximum delay spread is twice the one measured in the classical one-way channel in a similar environment [51], which is in line with the double convolution of the back-scattering channel impulse response.

Finally, we point out that the measurement data here discussed are the same used for R-SLAM purposes, which will be the subject of the next section. For the reader's convenience, the settings and parameters value adopted during the measurement campaigns are summarized in Table I.

#### E. Impact of the Scenario on THz R-SLAM.

When operating within the THz frequency range, it could be the case that signal blockage, which becomes increasingly

TABLE I  
MEASUREMENT CAMPAIGN: PARAMETERS AND SETTINGS

Description	Parameter	Value
Measurement setup		
Frequency sweep range	–	235-320 GHz
Frequency sweep step	–	10 MHz
Number of CIR samples	$M$	8501
Angular range	–	$[-90^\circ, 90^\circ]$
Angular steering step	–	$1^\circ$
Number of steering angles	$N$	181
Transmit antenna gain	$G_{TX}$	20 dBi
Receive antenna gain	$G_{RX}$	20 dBi
Half Power Beam Width	HPBW	$18^\circ$
Detection threshold	–	-100 dB
Delay resolution	$T_s$	1.56 ps
Measurement data processing		
NM algorithm threshold	$\eta_{CF}$	$10^{-2}$
GEM algorithm threshold	$\eta_{CL}$	0.4
Scan vector threshold	$\eta_{SV}$	0.9
Kalman filter parameters		
Power Spectral Density (PSD) of the linear acceleration noise	$w_0$	$10^{-4}$
PSD of the angular acceleration noise	$w_\theta$	$10^{-4}$
Time step	$T_F$	1 s
Position estimation error std	$\sigma_x = \sigma_y$	$4.7 \cdot 10^{-3}$ m
Angle estimation error std	$\sigma_\theta$	$1.7 \cdot 10^{-3}$ rad

significant at higher frequencies, may impede the detection of objects located further away and potentially obscured by closer ones [65]. In principle, this is a critical issue in the context of environment mapping, as it can result in incomplete representations of the environment. The simplest solution to this problem is to observe the environment from multiple locations and derive the map by leveraging all available measurements, as provided by our methodology. Conversely, the existence of many reflective objects within the sensed area is beneficial for the localization procedure, as it provides the localization algorithm with multiple landmarks that can be utilized to determine the radar's position. This, in turn, enhances the accuracy of mapping, which relies heavily on precise knowledge of the radar's location.

## VI. R-SLAM EXPERIMENTAL PERFORMANCE

In this section, we investigate the performance of the R-SLAM algorithms using the radar measurements as input. Since the state  $\mathbf{x}_k$  of the radar at instant  $k$  is estimated starting from relative pose estimations, the final estimated trajectory and map will be relative to its initial position.

The lower sections of Figs. 9, 10, and 11 show the estimated trajectories derived from measurements taken in the corresponding scenarios depicted in the upper sections of the same figures. These estimated trajectories are then compared to the ground-truth trajectory, represented by the cyan curve. To define the ground-truth trajectory, a reference system was established within the area, with its origin  $\mathbf{p}_0 = (x = 0, y = 0)$  aligned with position #1. The actual coordinates of the radar's placement were determined thanks to the positioner and a laser meter, ensuring an accuracy of 1 mm.

To aid the reader's comprehension of the measurement environment, let us clarify that the wall with the open door in

TABLE II  
TRAJECTORY ESTIMATION ROOT-MEAN-SQUARE ERROR (RMSE) FOR DIFFERENT APPROACHES AND SCENARIOS

	Scenario A	Scenario B	Scenario C
FM	5.7 mm	15 cm	24 cm
SFM	5 mm	15 cm	12 cm
LSM	6.5 cm	3.3 cm	74 cm

Fig. 6(a) corresponds to the rightmost vertical wall in Figs. 9 (top), 10 (top) and 11 (top), whereas the wall behind the wide desk in Fig. 6(b) corresponds to the upper horizontal wall in Figs. 9 (top), 10 (top) and 11 (top).

The radar trajectories have been estimated using the *Fourier-Mellin-based* (FM), *Simplified Fourier-Mellin* (SFM), and the *Laser Scan Matching* (LSM) algorithms for the relative pose estimation. A summary of the trajectory estimation RMSE for different approaches and scenarios is reported in Table II. The RMSE was calculated using the measured coordinates and those estimated by the algorithm as

$$\text{RMSE} = \sqrt{\frac{1}{N} \sum_{i=1}^N \|\mathbf{p}_i - \hat{\mathbf{p}}_i\|^2} \quad (37)$$

with  $N$  being the number of positions considered in each measurement campaign,  $\mathbf{p}_i$  and  $\hat{\mathbf{p}}_i$  the  $i$ th true and estimated positions of the radar, respectively.

All algorithms provide the best trajectory estimation performance in Scenario A depicted in Fig. 9 (the three estimated trajectories appear overlaid with the true trajectory), with a RMSE of 5.7 mm (FM), 5 mm (SFM), and 6.5 cm (LSM). According to the achieved results, the millimeter-level accuracy achieved with FM and SFM is of great interest.

Somewhat more challenging is Scenario B in Fig. 10, where the same trajectory is followed while keeping the radar pointed perpendicular to the direction of movement. In this case, the relative pose relies mainly on CIR variations in the angular domain that might be difficult to be recognized because variations in the incident angle of the electromagnetic waves on walls typically correspond to significant backscatter intensity fluctuations. As a consequence, the RMSEs are higher than those obtained in Scenario A, that is 15 cm (FM), 15 cm (SFM), and 3.3 cm (LSM), denoting a higher sensitivity of FM and SFM algorithms to this effect.

Finally, a more elaborated trajectory following an oval path is considered in Scenario C (Fig. 11), where simultaneous translations and rotations are present. The RMSEs of the trajectory estimation for the three algorithms are 24 cm (FM), 12 cm (SFM), and 74 cm (LSM). Surprisingly, the SFM algorithm outperforms the others, while the LSM algorithm exhibits a relatively high estimation error. This result can be attributed to the fact that, although FM should theoretically provide the best estimate of the relative pose, this holds true only in the case of perfect images, that is, those that precisely correspond to rotated and translated versions of each other. Unfortunately, radar images are far to be perfect because of multipath, noise, and the above-mentioned backscatter intensity fluctuations that create several artifacts. Since FM and the LSM algorithms involve much more

processing steps than SFM, the latter proves to be more robust to artifacts.

As far as the mapping is regarded, the color of the estimated map in Figs. 9 (bottom), 10 (bottom) and 11 (bottom) represents the occupancy status: black, grey, and white cells indicate the value of the belief at the end of the mapping process, being equal to 1 (occupied), 0.5 (complete uncertainty), or 0 (empty), respectively. Mapping has been obtained starting from the FM trajectory estimate. In fact, since all algorithms achieved cm-level accuracies, the maps obtained with SFM and LSM show no significant differences visually. As evident, the estimated maps are consistent with the actual shape of the considered scenario.

In conclusion, these experimental results validate the feasibility of R-SLAM using backscattered signals in the THz band collected by a mobile radar. Furthermore, they demonstrate the potential to achieve cm-level localization accuracy without the need for any dedicated infrastructure.

## VII. CONCLUSION

In this article, we presented an R-SLAM algorithm based on Fourier-Mellin transforms, together with its simplified version, which can operate with signals generated by a mobile radar. An ad-hoc measurement campaign was carried out in the THz band with the aim of characterizing the THz backscattering channel model and assessing the performance of the proposed R-SLAM algorithms in a real-world scenario. The numerical results demonstrate the feasibility of infrastructure-less localization and mapping with a *personal radar*, in the perspective of 6G systems where integrated communication, localization, and mapping capabilities will be a requirement. Future work will address the problem of absolute pose estimation and improve the robustness to artifacts in radar images. To this purpose, ultra-high gain antennas [66], with HPBW less than  $1^\circ$ , could be used to approximate a near-pencil beam behaviour and reduce the outliers and artifacts in radar measurements, in order to simplify the GEM pre-processing.

## REFERENCES

- [1] H. Saeed, N. Saeed, T. Y. Al-Naffouri, and M. -S. Alouini, "Next generation terahertz communications: A rendezvous of sensing, imaging, and localization," *IEEE Commun. Mag.*, vol. 58, no. 5, pp. 69–75, May 2020.
- [2] N. Rajatheva et al., "Scoring the terabit/s goal: Broadband connectivity in 6G," 2020, *arXiv:2008.07220*.
- [3] I. F. Akyildiz, J. M. Jornet, and C. Han, "Terahertz band: Next frontier for wireless communications," *Phys. Commun.*, vol. 12, pp. 16–32, 2014. [Online]. Available: <https://www.sciencedirect.com/science/article/pii/S1874490714000238>
- [4] I. F. Akyildiz and J. M. Jornet, "Realizing ultra-massive MIMO (1024×1024) communication in the (0.06–10) Terahertz band," *Nano Commun. Netw.*, vol. 8, pp. 46–54, 2016. [Online]. Available: <https://www.sciencedirect.com/science/article/pii/S1878778916000107>
- [5] I. F. Akyildiz, J. M. Jornet, and C. Han, "TeraNets: Ultra-broadband communication networks in the terahertz band," *IEEE Wireless Commun.*, vol. 21, no. 4, pp. 130–135, Aug. 2014.
- [6] J. Yang, C.-K. Wen, X. Yang, J. Xu, T. Du, and S. Jin, "Multi-domain cooperative SLAM: The enabler for integrated sensing and communications," *IEEE Wireless Commun.*, vol. 30, no. 1, pp. 40–49, Feb. 2023, doi: [10.1109/MWC.006.2200217](https://doi.org/10.1109/MWC.006.2200217).
- [7] A. Shafie, N. Yang, C. Han, J. M. Jornet, M. Juntti, and T. Kurner, "Terahertz communications for 6G and beyond wireless networks: Challenges, key advancements, and opportunities," *IEEE Netw.*, early access, Sep. 12, 2022, doi: [10.1109/MNET.118.2200057](https://doi.org/10.1109/MNET.118.2200057).
- [8] C. Chaccour, M. N. Soorki, W. Saad, M. Bennis, P. Popovski, and M. Debbah, "Seven defining features of terahertz (THz) wireless systems: A fellowship of communication and sensing," *IEEE Commun. Surveys Tut.*, vol. 24, no. 2, pp. 967–993, Secondquarter 2022.
- [9] C. Han et al., "Terahertz wireless channels: A holistic survey on measurement, modeling, and analysis," *IEEE Commun. Surveys Tut.*, vol. 24, no. 3, pp. 1670–1707, Thirdquarter 2022.
- [10] A. M. Elbir, K. V. Mishra, and S. Chatzinotas, "Terahertz-band joint ultra-massive MIMO radar-communications: Model-based and model-free hybrid beamforming," *IEEE J. Sel. Topics Signal Process.*, vol. 15, no. 6, pp. 1468–1483, Nov. 2021.
- [11] H. Chen, H. Saeed, T. Ballal, H. Wymeersch, M. -S. Alouini, and T. Y. Al-Naffouri, "A tutorial on terahertz-band localization for 6G communication systems," *IEEE Commun. Surveys Tut.*, vol. 24, no. 3, pp. 1780–1815, Thirdquarter 2022.
- [12] G. Pasolini et al., "Crowd-based cognitive perception of the physical world: Towards the internet of senses," *Sensors*, vol. 20, no. 9, 2020, Art. no. 2437.
- [13] C. Cadena et al., "Past, present, and future of simultaneous localization and mapping: Toward the robust-perception age," *IEEE Trans. Robot.*, vol. 32, no. 6, pp. 1309–1332, Dec. 2016.
- [14] H. Durrant-Whyte and T. Bailey, "Simultaneous localization and mapping: Part I," *IEEE Robot. Automat. Mag.*, vol. 13, no. 2, pp. 99–110, Jun. 2006.
- [15] S. Thrun and M. Montemerlo, "The graph SLAM algorithm with applications to large-scale mapping of urban structures," *Int. J. Robot. Res.*, vol. 25, no. 5/6, pp. 403–429, 2006.
- [16] N. Zeller, F. Quint, and U. Stilla, "From the calibration of a light-field camera to direct plenoptic odometry," *IEEE J. Sel. Topics Signal Process.*, vol. 11, no. 7, pp. 1004–1019, Oct. 2017.
- [17] Q. Fu et al., "Fast ORB-SLAM without keypoint descriptors," *IEEE Trans. Image Process.*, vol. 31, pp. 1433–1446, 2022.
- [18] F. Guidi, A. Guerra, and D. Dardari, "Personal mobile radars with millimeter-wave massive arrays for indoor mapping," *IEEE Trans. Mobile Comput.*, vol. 15, no. 6, pp. 1471–1484, Jun. 2016.
- [19] F. Guidi, A. Mariani, A. Guerra, D. Dardari, A. Clemente, and R. D'Errico, "Indoor environment-adaptive mapping with beamsteering massive arrays," *IEEE Trans. Veh. Tech.*, vol. 67, no. 10, pp. 10139–10143, Oct. 2018.
- [20] O. Li et al., "Integrated sensing and communication in 6G: A prototype of high resolution multichannel THz sensing on portable device," *EURASIP J. Wireless Commun. Netw.*, vol. 2022, no. 1, Oct. 2022, Art. no. 106. [Online]. Available: <https://doi.org/10.1186/s13638-022-02172-w>
- [21] M. Lotti et al., "Radio simultaneous localization and mapping in the terahertz band," in *Proc. 25th Int. ITG Workshop Smart Antennas*, 2021, pp. 1–6.
- [22] C. B. Barneto et al., "Millimeter-wave mobile sensing and environment mapping: Models, algorithms and validation," *IEEE Trans. Veh. Tech.*, vol. 71, no. 4, pp. 3900–3916, Apr. 2022.
- [23] Q.-S. Chen, M. Defrise, and F. Deconinck, "Symmetric phase-only matched filtering of Fourier-Mellin transforms for image registration and recognition," *IEEE Trans. Pattern Anal. Mach. Intell.*, vol. 16, no. 12, pp. 1156–1168, Dec. 1994.
- [24] B. S. Reddy and B. N. Chatterji, "An FFT-based technique for translation, rotation, and scale-invariant image registration," *IEEE Trans. Image Process.*, vol. 5, no. 8, pp. 1266–1271, Aug. 1996.
- [25] W. Hess, D. Kohler, H. Rapp, and D. Andor, "Real-time loop closure in 2D LIDAR SLAM," in *Proc. IEEE Int. Conf. Robot. Automat.*, 2016, pp. 1271–1278.
- [26] E. Leitinger, F. Meyer, F. Hlawatsch, K. Witrisal, F. Tufvesson, and M. Z. Win, "A belief propagation algorithm for multipath-based SLAM," *IEEE Trans. Wireless Commun.*, vol. 18, no. 12, pp. 5613–5629, Dec. 2019.
- [27] J. Mullane, B.-N. Vo, M. D. Adams, and B. -T. Vo, "A random-finite-set approach to Bayesian SLAM," *IEEE Trans. Robot.*, vol. 27, no. 2, pp. 268–282, Apr. 2011.
- [28] M. Montemerlo, S. Thrun, D. Koller, and B. Wegbreit, "FastSLAM: A factored solution to the simultaneous localization and mapping problem," in *Proc. 18th Nat. Conf. Artif. Intell.*, Edmonton, Alberta, Canada, 2002, pp. 593–598.
- [29] M. Holder, S. Hellwig, and H. Winner, "Real-time pose graph SLAM based on radar," in *Proc. IEEE Intell. Veh. Symp.*, 2019, pp. 1145–1151.
- [30] P. Checchin et al., "Radar scan matching SLAM using the Fourier-Mellin transform," in *Field and Service Robotics*. Berlin, Germany: Springer, 2010, pp. 151–161.
- [31] Z. Hong et al., "Radar SLAM: A robust SLAM system for all weather conditions," Apr. 2021, *arXiv:2104.05347*.

- [32] P. Mirowski et al., "SignalSLAM: Simultaneous localization and mapping with mixed WiFi, bluetooth, LTE and magnetic signals," in *Proc. Int. Conf. Indoor Positioning Indoor Navigation*, 2013, pp. 1–10.
- [33] H. Wymeersch and G. Seco-Granados, "Adaptive detection probability for mmWave 5 G SLAM," in *Proc. 2nd 6G Wireless Summit*, 2020, pp. 1–5.
- [34] H. Kim, K. Granström, L. Svensson, S. Kim, and H. Wymeersch, "PMBM-based SLAM filters in 5G mmwave vehicular networks," *IEEE Trans. Veh. Tech.*, vol. 71, no. 8, pp. 8646–8661, Aug. 2022.
- [35] Y. Ge et al., "A computationally efficient EK-PMBM filter for bistatic mmwave radio SLAM," *IEEE J. Sel. Areas Commun.*, vol. 40, no. 7, pp. 2179–2192, Jul. 2022.
- [36] C. B. Barneto, S. D. Liyanaarachchi, M. Heino, T. Riihonen, and M. Valkama, "Full duplex radio/radar technology: The enabler for advanced joint communication and sensing," *IEEE Wireless Commun.*, vol. 28, no. 1, pp. 82–88, Feb. 2021.
- [37] B. Jang and H. Kim, "Indoor positioning technologies without offline fingerprinting map: A survey," *IEEE Commun. Surveys Tut.*, vol. 21, no. 1, pp. 508–525, Firstquarter 2019.
- [38] H. Wymeersch, J. He, B. Denis, A. Clemente, and M. Juntti, "Radio localization and mapping with reconfigurable intelligent surfaces: Challenges, opportunities, and research directions," *IEEE Veh. Tech. Mag.*, vol. 15, no. 4, pp. 52–61, Dec. 2020.
- [39] Z. Yang et al., "MetaSLAM: Wireless simultaneous localization and mapping using reconfigurable intelligent surfaces," *IEEE Trans. Wireless Commun.*, vol. 22, no. 4, pp. 2606–2620, Apr. 2022.
- [40] K. Witrissal et al., "High-accuracy localization for assisted living: 5G systems will turn multipath channels from foe to friend," *IEEE Signal Process. Mag.*, vol. 33, no. 2, pp. 59–70, Mar. 2016.
- [41] M. Aladsani, A. Alkhateeb, and G. C. Trichopoulos, "Leveraging mmWave imaging and communications for simultaneous localization and mapping," in *Proc. ICASSP IEEE Int. Conf. Acoust., Speech Signal Process.*, 2019, pp. 4539–4543.
- [42] H. Kim, K. Granström, L. Gao, G. Battistelli, S. Kim, and H. Wymeersch, "5G mmWave cooperative positioning and mapping using multi-model PHD filter and map fusion," *IEEE Trans. Wireless Commun.*, vol. 19, no. 6, pp. 3782–3795, Jun. 2020.
- [43] Y. Ge et al., "5G SLAM using the clustering and assignment approach with diffuse multipath," *Sensors*, vol. 20, no. 16, 2020, Art. no. 4656.
- [44] C. B. Barneto et al., "Millimeter-wave mobile sensing and environment mapping: Models, algorithms and validation," *IEEE Trans. Veh. Technol.*, vol. 71, no. 4, pp. 3900–3916, 2022, doi: [10.1109/TVT.2022.3146003](https://doi.org/10.1109/TVT.2022.3146003).
- [45] J. Callmer et al., "Radar SLAM using visual features," *EURASIP J. Adv. Signal Process.*, vol. 2011, no. 1, pp. 1–11, 2011.
- [46] R. I. Stantchev et al., "Real-time terahertz imaging with a single-pixel detector," *Nature Commun.*, vol. 11, no. 1, pp. 1–8, 2020.
- [47] G. Valušis et al., "Roadmap of terahertz imaging 2021," *Sensors*, vol. 21, no. 12, 2021, Art. no. 4092.
- [48] P. Zheng, T. Ballal, H. Chen, H. Wymeersch, and T. Y. Al-Naffouri et al., "Coverage analysis of joint localization and communication in THz systems with 3D arrays," Oct. 2022, doi: [10.36227/techrxiv.21385080.v1](https://doi.org/10.36227/techrxiv.21385080.v1).
- [49] A. Batra, M. El-Absi, M. Wiemeler, D. Göhringer, and T. Kaiser, "Indoor THz SAR trajectory deviations effects and compensation with passive sub-mm localization system," *IEEE Access*, vol. 8, pp. 177519–177533, 2020.
- [50] L. Pometcu and R. D'Errico, "An indoor channel model for high data-rate communications in D-band," *IEEE Access*, vol. 8, pp. 9420–9433, 2020.
- [51] M. Lotti, M. Caillet, and R. D'Errico, "Comparison of indoor channel characteristics for Sub-THz bands from 125 GHz to 300 GHz," in *Proc. 16th Eur. Conf. Antennas Propag.*, 2022, pp. 1–5.
- [52] D. Serghiou, M. Khalily, T. W. C. Brown, and R. Tafazolli, "Terahertz channel propagation phenomena, measurement techniques and modeling for 6G wireless communication applications: A survey, open challenges and future research directions," *IEEE Commun. Surveys Tut.*, vol. 24, no. 4, pp. 1957–1996, Fourthquarter 2022.
- [53] S. Adibelli, P. Juyal, M. Prvulovic, and A. Zajic, "THz bistatic backscatter side-channel sensing at a distance," *IEEE Trans. Antennas Propag.*, vol. 70, no. 2, pp. 1440–1450, Feb. 2022.
- [54] A. Guerra, F. Guidi, J. Dall'Ara, and D. Dardari, "Occupancy grid mapping for personal radar applications," in *Proc. IEEE Statist. Signal Process. Workshop*, 2018, pp. 766–770.
- [55] I. F. Akyildiz, A. Kak, and S. Nie, "6G and beyond: The future of wireless communication systems," *IEEE Access*, vol. 8, pp. 133995–134030, 2020.
- [56] A.-A. A. Boulogeorgos et al., "Terahertz technologies to deliver optical network quality of experience in wireless systems beyond 5G," *IEEE Commun. Mag.*, vol. 56, no. 6, pp. 144–151, Jun. 2018.
- [57] M. C. Budge and S. R. German, *Basic Radar Analysis*. 2nd ed. Norwood, MA, USA: Artech House, 2020.
- [58] F. Guidi, A. Guerra, D. Dardari, A. Clemente, and R. D'Errico, "Joint energy detection and massive array design for localization and mapping," *IEEE Trans. Wireless Commun.*, vol. 16, no. 3, pp. 1359–1371, Mar. 2017.
- [59] Y. Bar-Shalom, X. R. Li, and T. Kirubarajan, *Estimation With Applications to Tracking and Navigation: Theory Algorithms and Software*. Hoboken, NJ, USA: Wiley, 2004.
- [60] D. Dardari, P. Closas, and P. M. Djurić, "Indoor tracking: Theory, methods, and technologies," *IEEE Trans. Veh. Tech.*, vol. 64, no. 4, pp. 1263–1278, Apr. 2015.
- [61] S. Thrun, "Learning metric-topological maps for indoor mobile robot navigation," *Artif. Intell.*, vol. 99, no. 1, pp. 21–71, 1998.
- [62] J. Clausen, "Branch and bound algorithms-principles and examples," *Dept. Comput. Sci., Univ. Copenhagen*, pp. 1–30, 1999.
- [63] K. Haneda, J. Järveläinen, A. Karttunen, M. Kyrö, and J. Putkonen, "A statistical spatio-temporal radio channel model for large indoor environments at 60 and 70 GHz," *IEEE Trans. Antennas Propag.*, vol. 63, no. 6, pp. 2694–2704, Jun. 2015.
- [64] B. Fleury, "First- and second-order characterization of direction dispersion and space selectivity in the radio channel," *IEEE Trans. Inf. Theory*, vol. 46, no. 6, pp. 2027–2044, Sep. 2000.
- [65] M. Lotti, M. Caillet, and R. D'Errico, "Multiband sub-THz double angular characterization in indoor scenario," *IEEE Trans. Antennas Propag.*, vol. 71, no. 2, pp. 1747–1756, Feb. 2023.
- [66] O. Koutsos et al., "Ultra-high gain transmitarray antenna for wireless backhauling at 280 GHz," in *Proc. 47th Int. Conf. Infrared, Millimeter Terahertz Waves*, 2022, pp. 1–2.



**Marina Lotti** (Graduate Student Member, IEEE) received the B.S. and the M.S. (*cum laude*) degrees in electronics and telecommunication engineering from the University of Bologna, Italy, in 2017 and 2020, respectively. She is currently working towards the Ph.D. degree in smart radio environments exploiting reconfigurable intelligent surfaces. From 2020 to 2021, she was a Research Engineer with CEA-Leti, France, working on channel characterizations in the sub-THz frequency range and radar measurements for localization and mapping purposes.



**Gianni Pasolini** (Member, IEEE) received the M.Sc. degree in telecommunications engineering and the Ph.D. degree in electronic engineering and computer science from the University of Bologna, Bologna, Italy, in 1999 and 2003, respectively. He is currently an Associate Professor with the Department of Electrical, Electronic and Information Engineering, University of Bologna, where he has been teaching various courses in the field of telecommunications since 2003. His research interests include wireless communication systems, Internet of Things, digital signal processing, and THz communications. He was the recipient of the Best Paper Award at the 2023 IEEE International Conference on Communications (ICC). Throughout his career, he has actively participated in several European initiatives focused on wireless communications, including COST actions and Networks of Excellence. He is an Associate Editor for IEEE OPEN JOURNAL OF THE COMMUNICATIONS SOCIETY (IEEE OJ-COM). He was a member of the Organizing Committee for the 2018 IEEE International Symposium on Personal, Indoor and Mobile Radio Communications (PIMRC), the 2017 IEEE International Symposium on Wireless Communication Systems (ISWCS), and the 2011 IEEE International Conference on Ultra-Wideband (ICUWB). He is one of the founding members of the National Laboratory of Wireless Communications - Wilab of the National Inter-University Consortium for Telecommunications (CNIT) in Italy.



**Anna Guerra** (Member, IEEE) received the B.S. and M.S. degrees in electronics and telecommunications engineering and the Ph.D. degree in electronics, telecommunications, and information technologies from the University of Bologna, Bologna, Italy, in 2009, 2011, and 2016, respectively. From 2016 to 2021, she has been a Postdoctoral Researcher with the University of Bologna. Since 2021, she has been a Researcher with the National Research Council (CNR) of Italy. Since 2022, she has been an Adjunct Professor with the University of Ferrara, Ferrara, Italy.

From 2018 to 2020, she received a global Marie Skłodowska-Curie Research Fellowship for the H2020 AirSens project, and she spent the project's outgoing phase at Stony Brook University, Stony Brook, NY, USA. She was the recipient of the Best Student Paper Award at the 2014 IEEE International Conference on Ultra-Wideband held in Paris, France, and the Best Paper Awards at the 2019 IEEE RFID-TA Conference, Pisa, and at the 2021 IEEE International Conference on Autonomous Systems, Montreal, QC, Canada. She is an Associate Editor for the IEEE COMMUNICATIONS LETTERS and IEEE WIRELESS COMMUNICATIONS LETTERS.



**Francesco Guidi** (Member, IEEE) received the B.S. and M.S. degrees (*summa cum laude*) in biomedical and in electronics and telecommunications engineering from the University of Bologna, Bologna, Italy, in 2006 and 2009, respectively, and the joint Ph.D. degree in electronics, telecommunications and information technologies from Ecole Polytechnique ParisTech, Palaiseau, France, and from the University of Bologna, in 2013. He is currently a Researcher with IEIIT-CNR, Italy. From 2013 to 2015, he was a Postdoctoral Researcher with the University of

Bologna. His research interests include RFID and radar technologies, joint antenna and channel characterization, signal processing, UWB and mm-waves technologies. From 2015 to 2017, he was the recipient of an individual European Marie Skłodowska-Curie Fellowship at French Atomic Energy Commission (CEA-LETI), Grenoble, France. He was also the recipient of the Best Student Paper Award at the 2014 IEEE International Conference on Ultra-Wideband, and the Best Paper Award at the 2021 IEEE International Conference on Autonomous Systems, Montreal, Canada. Dr. Guidi has organized a number of Special Sessions and Workshop at International Conferences, and is an Associate Editor for IEEE WIRELESS COMMUNICATIONS LETTERS.



**Raffaele D'Errico** (Senior Member, IEEE) received the Laurea degree (*summa cum laude*) in telecommunications engineering from the University of Bologna, Bologna, Italy, in 2005, and the Ph.D. degree from the University of Orsay, Paris, France, and University of Bologna, in 2008. Since 2008 he has been a Research Engineer and Project Manager with CEA-LETI. His research interests include propagation channel sounding and modelling 6G/5G networks, mm-wave communications, RIS, wireless sensor networks, Body Area Networks (BANs), antenna design and character-

ization, RFID, UWB localization, radar and Over-The-Air tests. He has been involved in several FP7, H2020 and ANR projects. He participated in COST 2100 and IC1004 activities, IRACON action on 5G and beyond networks. He is VP of U.R.S.I. France commission F on propagation. He was the recipient of Best Paper Awards at IEEE PIMRC 2009, IFP NTMS 2011, and LAPC 2012.



**Davide Dardari** (Senior Member, IEEE) is currently a Full Professor with the University of Bologna, Bologna, Italy. He has been a Research Affiliate with the Massachusetts Institute of Technology, Cambridge, MA, USA. He has authored or coauthored more than 250 technical articles and played several important roles in various national and European projects. His research interests include wireless communications, localization techniques, smart radio environments, and distributed signal processing. He was the recipient of the IEEE Aerospace and Electronic

Systems Society M. Barry Carlton Award in 2011 and the IEEE Communications Society Fred W. Ellersick Prize in 2012. He was the Chair of the Radio Communications Committee of the IEEE Communications Society. He was the Co-General Chair of the 2011 IEEE International Conference on Ultra-Wideband and a Co-Organizer of IEEE International Workshop on Advances in Network Localization and Navigation (ANLN) ICC 2013-2016 editions. He was also the TPC Chair of IEEE International Symposium on Personal, Indoor and Mobile Radio Communications (PIMRC 2018), TPC Co-Chair of the Wireless Communications Symposium of the 2007/2017 IEEE International Conference on Communications, and the TPC Co-Chair of the 2006 IEEE International Conference on Ultra-Wideband. He was the Editor of IEEE TRANSACTION ON WIRELESS COMMUNICATIONS from 2006 to 2012 and the guest editor for several journals. Currently, he is a Senior Member of the Editorial Board of the IEEE Signal Processing Magazine. He was a Distinguished Lecturer of IEEE Communication Society from 2018 to 2019.